Characterization of Integrated Optical Strain Sensors Based on Silicon Waveguides

Wouter J. Westerveld, *Member, IEEE*, Suzanne M. Leinders, Pim M. Muilwijk, Jose Pozo, *Member, IEEE*, Teun C. van den Dool, Martin D. Verweij, *Member, IEEE*, Mirvais Yousefi, *Member, IEEE*, and H. Paul Urbach

***Abstract*—Microscale strain gauges are widely used in micro electro-mechanical systems (MEMS) to measure strains such as those induced by force, acceleration, pressure or sound. We propose all-optical strain sensors based on micro-ring resonators to be integrated with MEMS. We characterized the strain-induced shift of the resonances of such devices. Depending on the width of the waveguide and the orientation of the silicon crystal, the linear wavelength shift per applied strain varies between 0.5 and 0.75 pm/microstrain for infrared light around 1550 nm wavelength. The influence of the increasing ring circumference is about three times larger than the influence of the change in waveguide effective index, and the two effects oppose each other. The strong dispersion in 220 nm high silicon sub-wavelength waveguides accounts for a decrease in sensitivity of a factor 2.2 to 1.4 for waveguide widths of 310 nm to 860 nm. These figures and insights are necessary for the design of strain sensors based on silicon waveguides.**

***Index Terms*—Optical sensors, strain measurement, silicon-on-insulator, integrated optics, optical waveguide, microsensors, mechanical sensors.**

I. Introduction

MICROSCALE strain gauges are widely used in micro electro-mechanical systems (MEMS) to measure strains such as those induced by force, acceleration, pressure or (ultra)sound [1], [2]. These sensors are traditionally based on a piezoresistive or piezoelectric material which transduces the strain to an electrical signal. Alternatively, optical resonators can be used as sensing element, providing particular benefits: high-speed readout, small sensor size, small multiplexer size (1 mm^2), insensitivity to electromagnetic interference, and no danger of igniting gas explosions with electric sparks.

Integrated optics technology allows the optical strain sensors, as well as their multiplexing circuit, to be integrated with MEMS. The sensing elements and their multiplexers can often be fabricated in a single processing step. Silicon-on-insulator (SOI) has emerged as one of the focus platforms for integrated optics, and is relatively straightforward to integrate with MEMS, as MEMS are most commonly made of silicon. Micro-electronic research institutes have tailored CMOS fabrication processes to the demands of SOI optical circuits, and now offer cheap and reproducible wafer-scale fabrication [3], [4]. The high refractive index contrast of SOI ridge waveguides allows for a small device footprint, and single-mode guides have a cross section of only 400 nm $\times$ 220 nm.

We employ ring resonators as sensing element. Such a resonator consists of a waveguide which is looped, forming a closed cavity which has specific optical resonance wavelengths. Any change in the size or in the refractive index of this waveguide shifts its resonances, and this shift can be accurately recorded.

Several groups have reported on sensor micro opto-electro-mechanical systems (MOEMS) that are based on silicon integrated optical ring resonators, such as strain gauges [5], [6], or pressure sensors [7]–[9]. An application of particular interest is as ultrasound sensor for medical intravascular ultrasonography (IVUS). IVUS has been recommended for the diagnostics of atherosclerosis [10], [11]. IVUS is an invasive technique for blood vessel imaging where the sensor is attached to a catheter and brought inside the artery. Using an array of sensors improves the image quality but wiring many piezoelectric sensors with coaxial cables requires too much space for this application. As solution, we proposed a micro-machined ultrasound transducer with optical readout [12]. This sensor consists of a silicon ring resonator integrated in a membrane that deforms due to ultrasonic waves. Integrated optical multiplexers allow high-speed read-out of many sensors via one optical fiber and, moreover, insensitivity to electromagnetic interference allows usage inside MRI scanners.

The relation between strain and silicon waveguides is of broader interest than sensing. Electro-mechanical modulation of silicon optical resonators may be employed to modulate optical signals, for application in the field of telecommunication [13]. As alternative to silicon waveguide-based ring resonators, it is also possible to use photonic crystals cavities, which have their own dispersion relations [14]. Strain has also been used to modify the birefringence of larger SOI rib waveguides [15].

Manuscript received September 27, 2013; revised November 1, 2013; accepted November 3, 2013. Date of publication November 7, 2013; date of current version January 10, 2014. This work was supported by the TNO and the IOP Photonic Devices program of NL Agency.

W. J. Westerveld is with the Optics Research Group, Faculty of Applied Sciences, Delft University of Technology, 2628CH Delft, The Netherlands and also with the TNO, 2628CK Delft, The Netherlands (e-mail: w.j.westerveld@tudelft.nl).

S. M. Leinders and M. D. Verweij are with the Laboratory of Acoustical Wavefield Imaging, Faculty of Applied Sciences, Delft University of Technology, 2628CH Delft, The Netherlands (e-mail: S.M.Leinders@tudelft.nl; M.D.Verweij@tudelft.nl).

P. M. Muilwijk, J. Pozo, and T. C. van den Dool are with the TNO, 2628CK Delft, The Netherlands (e-mail: pim.muilwijk@tno.nl; jose.pozo@tno.nl; teun.vandendool@tno.nl).

M. Yousefi is with the Photonic Sensing Solutions, 1013EN Amsterdam, The Netherlands (e-mail: m.yousefi@photonics2.com).

H. P. Urbach is with the Optics Research Group, Faculty of Applied Sciences, Delft University of Technology, 2628CH Delft, The Netherlands (e-mail: h.p.urbach@udelft.nl).

Color versions of one or more of the figures in this paper are available online at http://ieeexplore.ieee.org.

Digital Object Identifier 10.1109/JSTQE.2013.2289992

1077-260X © 2013 IEEE. Personal use is permitted, but republication/redistribution requires IEEE permission.
See http://www.ieee.org/publications_standards/publications/rights/index.html for more information.

Strain is inevitable when using silicon photonic circuits on a flexible substrate [16]. Another interesting field of research is the strain-induced change in the electronic band-gap and the optical refractive index of silicon, with the possibility to introduce second-order nonlinearity [17]–[19]. However, details of the relation between an applied strain and the shift in optical resonance of ring resonators have not been studied.

We characterized the shift of the resonance wavelengths which is caused by a well-defined strain. This includes a characterization of the change in the effective index of the sub-wavelength silicon waveguide. We studied the influence of the waveguide width and the influence of the orientation of the silicon crystal. This knowledge is required for the design of mechanical sensors based on silicon integrated optics, such as ring resonators or Mach–Zehnder interferometers. Also, we quantified the contribution of three physical effects: the strain-induced change in circumference of the resonator, the strain-induced change in effective index of the waveguide, and the dispersion which is strong in sub-wavelength silicon waveguides.

This paper is organized as follows: first we present the devices which are used to study the effect of strain on silicon optical waveguides (see Section II), then we derive opto-mechanical theory describing these devices (see Section III), after which we detail the experimental setup and methodology (see Section IV). The characterization and the analysis of the devices are presented in Sections V and VI, respectively, and we conclude in Section VII.

II. Devices

In this section, we first describe the SOI-technology in which the devices are fabricated, secondly detail the ring resonators and then describe the sets of devices that we studied.

The integrated optical devices are in silicon-on-insulator technology, with 220 nm thick waveguides of mono-crystalline silicon. The guides are on top of a 2 μm thick buried oxide (BOX) layer which is on top of a 675 μm thick silicon substrate. We deposited a 2 μm thick SiO_2 cladding layer using plasma-enhanced chemical vapor deposition (PEVCD), so that the silicon waveguides are embedded in silica. The devices were fabricated via the EU-funded ePIXfab consortium at IMEC (Leuven, Belgium) [3], [4]. IMEC fabricated the devices in their CMOS line with 193 nm deep-UV lithography. The waveguides are not exactly rectangular but have a side-wall-angle of 10°. We measured the average widths of the fabricated waveguides with a helium ion microscope (Carl Zeiss SMT), providing an accuracy of 15 nm.

We designed long racetrack-shaped ring resonators in an "add-drop" configuration (see Fig. 1), and excite the "input" waveguide with infrared light with wavelengths λ around a center wavelength λ_c of 1550 nm. A directional coupler couples light from the "input/output" waveguide to the resonator, and an identical coupler is used half-way the racetrack to couple light to a "drop" waveguide. The transmitted spectrum $T(\lambda)$ in the "output" port has dips at the resonance wavelengths of the resonator. We characterized the couplers and 59% of the power is coupled from the waveguide to the track, such that the power which goes straight through the coupler $|t|^2 = 41\%$. Having a strong coupling in a symmetric add-drop configuration gives resonance dips with good extinction ratio even for high losses in the racetrack or for variations in coupling (e.g., due to fabrication) [20].

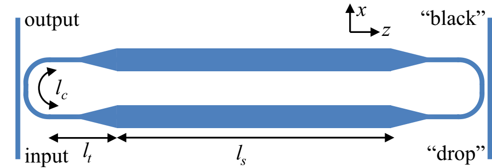

Fig. 1. Sketch of racetrack resonator with in/output ports (not to scale). Long straight waveguide has length $l_s = 1000$ μm and width w. Taper section has length $l_t = 64.35$ μm (4.35 μm long waveguide of width 400 nm, taper with a length varying from 0 to 60 μm, followed by a waveguide of width w to close the space.) Coupler section has length l_c and consists of two 10 μm long parallel guides (width ∼400 nm, gap 220 nm), and bends with a radius of 5 μm.

Silicon is anisotropic, so its deformation depends on the direction in which a force is applied. Therefore two sets of devices were fabricated and characterized; one with the long side of the racetrack parallel to the $\langle 110\rangle$ direction of the silicon crystal and one with the long side parallel to the $\langle 100\rangle$ direction of the silicon crystal. Reference [21] explains the crystal planes in a "(100) wafer" as we used. We characterized the influence of the width of the waveguide on the shift in resonance, therefore each set of devices consists of resonators with waveguide widths varying from 310 nm up to 860 nm.

III. Theory

This section presents the theory of ring resonators such as presented in the previous section, i.e., a looped waveguide with a varying width. First, Section III-A presents the optical theory of ring resonators, then Section III-B derives the opto-mechanical theory. Section III-C applies the theory to the long racetrack resonators under study. The relations derived in this section are used as fitting function of the measured spectra, and as basis for the analysis of the measurements.

A. Ring and Racetrack Resonators

The transmitted optical power T of a micro-ring resonator with two lossless couplers in an add-drop configuration such as shown in Fig. 1 is [20]

$$T = \frac{\alpha^2|t|^2 + |t|^2 - 2\alpha|t|^2\cos(\delta)}{1 + \alpha^2|t|^4 - 2\alpha|t|^2\cos(\delta)} \quad (1)$$

where $|t|^2$ is the straight-through power of the coupler and α^2 is the power transmission due to one round-trip through the ring ($\alpha = 1$ means zero loss). T thus describes the optical power transmitted from the input to the output of the connecting waveguide, and is wavelength dependent because δ is wavelength-dependent. The phase delay δ of one round-trip through the ring (including passing the couplers) is

$$\delta = \oint n_e(\rho,\lambda)\frac{2\pi}{\lambda}\mathrm{d}\rho = \langle n_e(\lambda)\rangle\frac{2\pi}{\lambda}l \quad (2)$$

where the waveguide effective index $n_e(\rho, \lambda)$ is averaged over the position ρ in the track with circumference l as $\langle n_e(\lambda)\rangle \equiv \frac{1}{l}\oint n_e(\rho,\lambda)\mathrm{d}\rho$. The effective index in the coupler is approximated equal to the effective index of a single isolated waveguide. The strong modal dispersion in sub-wavelength silicon waveguides is approximated to be linear around the center wavelength λ_c, and is expressed in terms of the effective group index $n_g \equiv n_e - \lambda\frac{\partial n_e}{\partial \lambda}$, so

$$n_e(\rho,\lambda) = n_e(\rho) + \big(n_e(\rho) - n_g(\rho)\big)\left(\frac{\lambda}{\lambda_c} - 1\right) \quad (3)$$

where n_e and n_g at the right-hand side, denoted without λ dependence, are evaluated at λ_c. As λ and ρ are independent

$$\langle n_e(\lambda)\rangle = \langle n_e\rangle + (\langle n_e\rangle - \langle n_g\rangle)\left(\frac{\lambda}{\lambda_c} - 1\right) \quad (4)$$

from which it is observed that the transmission spectrum of a racetrack resonator with varying width is described by the same relation as a resonator with a single waveguide, but with averaged effective index $\langle n_e\rangle$ and group index $\langle n_g\rangle$.

Equation (1) with (2) and (4) will be fitted to the measured resonance spectra to accurately obtain $\langle n_g\rangle$ and $\langle n_e\rangle$, from which the resonance wavelengths are calculated.

B. Strain-Induced Resonance Shift of Ring Resonators

This section details the shift in the resonances of a ring resonator due to an applied mechanical strain. Four physical effects play a role when elongating a ring- or racetrack resonator. First, the circumference of the track l increases. Second, the cross section of the waveguide shrinks due to the Poisson effect. Third, the refractive indices of the silicon and SiO_2 change due to the photo-elastic effect. The latter two effects together influence the effective index n_e of the waveguide. Fourth, the shift in resonance is affected by the dispersion in the waveguide.

In our case, a homogeneous strain S_z is applied parallel to the long sides of the racetrack resonator (the *z*-direction). The transmitted spectrum of the connecting waveguide shows dips at the resonance wavelengths λ_m when $\delta = m2\pi$, or

$$m\lambda_m = \oint n_e(\rho,\lambda_m,S_z)\left(1 + S_\rho(\rho,S_z)\right)\mathrm{d}\rho. \quad (5)$$

The effective index of the waveguide depends on a mechanical deformation. The local strain in the direction of the track S_ρ is taken into account by stretching each element $\mathrm{d}\rho$ to $(1+S_\rho)\mathrm{d}\rho$. For the straight waveguide of the racetracks as in Fig. 1, the *z*- and ρ-directions coincide, whereas they do not for the coupler section. We found that the relation between an applied strain S_z and the shift in resonance wavelength is linear, which is explained by the fact that the applied strains are small. A description of this linear influence can be found by taking the first derivative of (5) with respect to S_z,

$$m\frac{\partial\lambda_m}{\partial S_z} = \oint\left\{\left(\frac{\partial n_e}{\partial S_z} + \frac{\partial n_e}{\partial \lambda_m}\frac{\partial \lambda_m}{\partial S_z}\right)(1+S_\rho) + n_e\frac{\partial S_\rho}{\partial S_z}\right\}\mathrm{d}\rho$$

which we evaluate at zero strain (i.e., $S_z = S_\rho = 0$). Solving this equation for $\partial\lambda_m/\partial S_z$, substituting m from (5), and dividing by track circumference l gives

$$\frac{\partial\lambda_m}{\partial S_z} = \frac{\lambda_c}{\langle n_g\rangle l}\oint\left(\frac{\partial n_e}{\partial S_z} + n_e\frac{\partial S_\rho}{\partial S_z}\right)\mathrm{d}\rho \quad (6)$$

with λ_c the resonance wavelength λ_m without deformation. This equation is easiest understood when considering a resonator with a single waveguide shape (i.e., $\langle n_e\rangle = n_e$ and $\langle n_g\rangle = n_g$). In that case,

$$\frac{\partial\lambda_m}{\partial S_z} = \underbrace{\frac{n_e}{n_g}}_{\text{dispersion}}\left\langle \underbrace{\frac{\lambda_c}{n_e}\frac{\partial n_e}{\partial S_z}}_{\text{eff.index}} + \underbrace{\lambda_c\frac{\partial S_\rho}{\partial S_z}}_{\text{track-length}}\right\rangle \quad (7)$$

where the influence of the different physical effects are indicated. Without dispersion, $n_e/n_g = 1$. For the part of the track which is in the direction of the applied strain $S_\rho = S_z$, so $\partial S_\rho/\partial S_z = 1$, hence the contribution of the track-length change is simply λ_c.

C. Strain-Induced Resonance Shift of Long Racetracks

We measured very long racetracks because this will allow for neglecting the influence of the tapers and the couplers. In the long racetrack resonators, Equation (5) reads

$$m\lambda_m = 2l_s n_s(1+S_z) + \int_{\text{tapers}} n_e\,(1+S_\rho)\,\mathrm{d}\rho + \int_{\text{couplers}} n_e\,(1+S_\rho)\,\mathrm{d}\rho \quad (8)$$

where the contributions of the different sections of the track are separated (see Fig. 1, with l_s, l_t, and l_c indicating the straight, taper, and coupler sections, respectively) and n_s is the effective index of the long straight waveguide. We calculate the first-order influence of strain on this racetrack similarly to (6), and rewrite the equation such that the influence of the tapers and the couplers is written as a correction to the shift caused by the long straight guides

$$\begin{aligned}\langle n_g\rangle\frac{\partial\lambda_m}{\partial S_z} &= \lambda_c\left(\frac{\partial n_s}{\partial S_z} + n_s\right)\\ &\quad + \frac{\lambda_c}{l}\int_{\text{tapers}}\left(\frac{\partial n_e}{\partial S_z} + n_e\frac{\partial S_\rho}{\partial S_z} - \frac{\partial n_s}{\partial S_z} - n_s\right)\mathrm{d}\rho\\ &\quad + \frac{\lambda_c}{l}\int_{\text{couplers}}\left(\frac{\partial n_e}{\partial S_z} + n_e\frac{\partial S_\rho}{\partial S_z} - \frac{\partial n_s}{\partial S_z} - n_s\right)\mathrm{d}\rho.\end{aligned} \quad (9)$$

We will justify later that the second and third term of the right-hand side of this equation are small compared to the first one, and hence can be neglected, resulting in

$$\langle n_g\rangle\frac{\partial\lambda_m}{\partial S_z} \approx \lambda_c\left(\frac{\partial n_s}{\partial S_z} + n_s\right). \quad (10)$$

The taper is a waveguide in the *z*-direction with a width varying from 400 nm up to the width w of the long section waveguide. The second term at the right-hand side of (9) is the relative contribution of the taper to the resonance shift, with respect to the contribution of a waveguide with width w of the same

length. The relative contribution of the taper is smaller than the relative contribution of a 400 nm wide waveguide of the same length. Using (10), it is thus found that the second term of the right-hand side of (9) is smaller than

$$\frac{4l_t}{l}\left|\underbrace{\langle n_g\rangle\frac{\partial\lambda_m}{\partial S_z}}_{\text{width under study}}-\underbrace{\langle n_g\rangle\frac{\partial\lambda_m}{\partial S_z}}_{\text{width 400 nm}}\right|. \tag{11}$$

The third term of (9) comes from the effect of the couplers including the bend waveguides. This contribution can be either positive (as for the long waveguides) or negative (as the path-length might shrink due to the Poisson effect). We expect the magnitude to be smaller than twice the effect of a straight waveguide of equal length that is strained in its long direction. Thus the third term in (9) is smaller in magnitude than

$$2\frac{2l_c}{l}\left(\langle n_g\rangle\frac{\partial\lambda_m}{\partial S_z}\right). \tag{12}$$

As will be shown in Section V, the maximum measured difference in $\langle n_g\rangle(\partial\lambda_m/\partial S_z)$ for the devices under study with different waveguide widths is 10%. For these long racetracks, $4l_t/l = 11\%$, so the second term in (9) is smaller than 1.1%. The third term is smaller than $4l_c/l = 5\%$. Equation (10) is used in the characterization of the measurements. We characterized both $\langle n_g\rangle$ and $\partial\lambda_m/\partial S_z$. The effective index of the straight waveguide n_s is computed with a numerical mode solver, which allows us to extract the strain-induced change in effective index.

Similar to (7) in the more general Section III-B, we indicate the effects of the different phenomena in (10)

$$\frac{\partial\lambda_m}{\partial S_z}=\underbrace{\frac{n_s}{\langle n_g\rangle}}_{\text{dispersion}}\left(\underbrace{\frac{\lambda_c}{n_s}\frac{\partial n_s}{\partial S_z}}_{\text{eff.index}}+\underbrace{\lambda_c}_{\text{track-length}}\right). \tag{13}$$

This result is used in the interpretation of the measurements in Section VI. In fact, track-averaged group index $\langle n_g\rangle$ can be approximated as the group index n_g of the straight waveguide. We have used the numerical mode solver to show that this approximation is valid within 1%. In our analysis, we use the track-averaged group index which was accurately measured.

IV. Methodology

We characterized the photonic chips in an automated setup in which they are bent such that the top layer with the racetrack resonators is strained. Transmission spectra of the resonators were recorded for elongations varying from 0 to 275 microstrain. As example, Fig. 2(a) shows a resonance dip of the measured spectra for increasing strain. The resonance wavelengths, and the group index n_g, were extracted from fitting a relation for ring resonator transmission. Fig. 2(b) shows the resonance wavelength λ_m plotted versus the applied strain.

A. Mechanical Setup: Four Point Bending

We designed and fabricated a mechanical setup in which the chips are bent such that the top layer with the photonic circuit is uniformly strained (see Fig. 3). The setup is equipped with elastic elements to provide an accurate bending moment to the

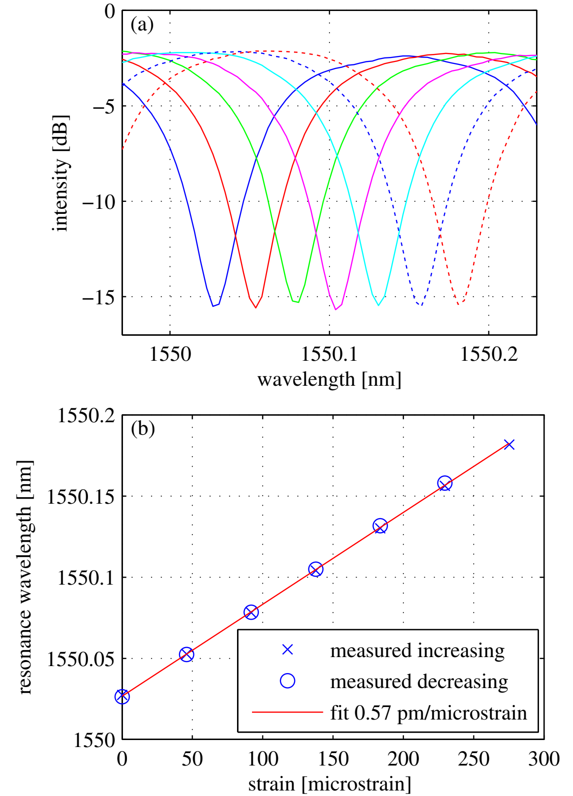

Fig. 2. Example of resonance shift due to an applied strain. (a) Small span of 7 measured spectra for increasing values of applied strain. Resonance dips shift to the red. Racetrack in the $\langle 1\,0\,0\rangle$ crystalline direction, with waveguide width 400 nm. (b) The wavelengths of the resonance dips λ_m in (a) is plotted versus the applied strain S_z. The wavelengths of the resonance dips for decreasing values of strain are also plotted. Resonance shift $\partial\lambda_m/\partial S_z$ is obtained from a linear fit.

chip, without hysteresis or other non-linearities. Between the two inner supports, the chip experiences a constant bending moment M (known as *pure bending*) [22]

$$M=\frac{a_1(a_4-a_3)}{4a_2}L \tag{14}$$

with L the load applied at the lever. The bending of the chip is described by plate bending theory for *thin plates with small deflections* [23], as its thickness H is small compared to its width W and length. An assumption in this theory is that the normal stresses in the *x*-direction can be neglected, so that there is no strain S_x in the *x*-direction and the width W of the chip does not change due to the applied load. In the setup, the deflection of the chip at considerable distance from its ends can be assumed to be cylindrical. In this mechanical analysis the influence of upper layers of the chip (BOX layer, waveguide layer, and cladding layer) is neglected as their total thickness of 4.220 μm is much smaller than the chip thickness of 675 μm. Hooke's law and plate bending theory give the relation between the stress σ_z and strain S_z in the chip [21], [23]:

$$\sigma_z=\frac{E_z}{1-\nu_{xz}\nu_{zx}}S_z \tag{15}$$

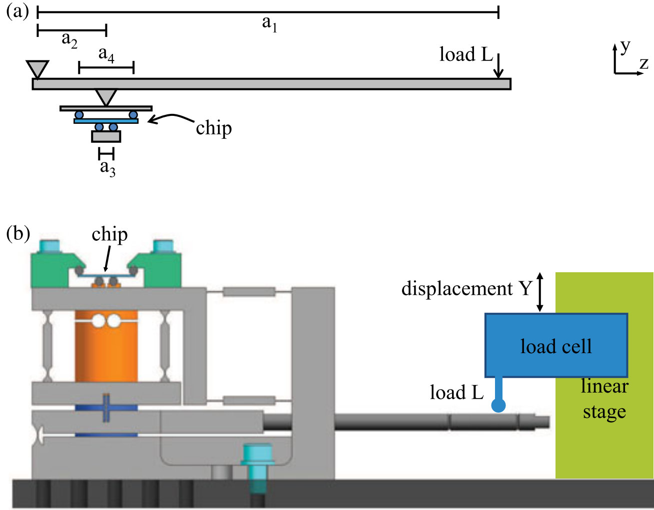

Fig. 3. (a) Analysis of the mechanical setup. (b) Sketch of the mechanical setup. Composed of the CAD drawing that was used to fabricate the setup (left-hand side), and a sketch of the linear stage with the load cell.

with Young's modulus[1] E_z and anisotropic Poisson's ratios[2] ν_{xz} and ν_{zx}. Combining (14) and (15) with the cylindrical deflection of the chip gives the strain S_z on the top surface of the chip in the mechanical setup

$$S_z = \frac{3a_1(a_4 - a_3)(1 - \nu_{xz}\nu_{zx})}{2a_2 W H^2 E_z} L. \tag{16}$$

A precise linear stage (Newport MFA-CC) applies a force to the lever, while a load cell (Omega LECB5) measures the actual applied load L. It was observed that the relation between the displacement of the linear stage Y and the applied load L is linear in the regime of our measurements, and also that the repeatability of the linear stage position Y was higher than the repeatability of the load cell. Therefore, we extracted a single number for the resistance of the chip to bending, $\partial Y/\partial L$, from all the measurements performed on a chip.

B. Optical Setup

The transmission spectra of the racetracks were measured with near infrared light around $\lambda_c = 1550$ nm. An amplified spontaneous emission light-source (OptoLink C-band ASE) was used to emit this light, and a 5 nm span of the spectra were recorded with an optical spectrum analyzer (OSA) (Yokogawa AQ6370B). The input and output waveguides of the racetrack resonators are routed to out-of-plane grating couplers at convenient locations on the chip, and coupled to cleaved optical fibers via free-space [24], [25]. These fibers were mounted on stages with piezo positioning, and automatically actively aligned in the horizontal (*x*,*z*)-plane before recording a spectrum. All transmission spectra are normalized to the transmission spectrum of a reference waveguide, which was smoothed by convolution with a 1 nm wide Gaussian window to remove Fabry–Pérot resonances originating from reflections of the out-of-plane grating couples.

A relation for ring resonator transmittance, Equations (1)–(4), was fitted to the recorded spectrum. The ring length l and straight-through power of the coupler $|t|^2 = 41\%$ were fixed, while the effective index $\langle n_e \rangle$, group index $\langle n_g \rangle$, resonator waveguide loss α^2 and fiber-coupling loss were fitted. The resolution bandwidth of the OSA was incorporated in this fitting by convoluting the calculated spectrum with a 20 pm wide Gaussian curve. For the zero-strain measurement, the mode number m of the resonance closest to λ_c was estimated from (5) where the effective index $n_e(\rho, \lambda_c, 0)$ was calculated using a mode solver (film mode matching method in FimmWave by PhotonDesign [26]). This dip was followed over consecutive measurements. An accurate initial guess of $\langle n_e \rangle$ and $\langle n_g \rangle$ (thus the wavelengths of the resonance dips) is necessary for the Levenberg–Marquardt fitting algorithm [27]. Therefore, the resonance dips were first found using *findpeaks* [28] and from this $\langle n_e \rangle$ and $\langle n_g \rangle$ were estimated via (5). This initial estimate allows for automated fitting of the spectra. With this fitting, the free parameters in (1)–(4) could be obtained, and λ_m was calculated from (5) with an accuracy much higher than the resolution bandwidth of the OSA.

C. Measurements

We characterized chips with the racetracks in the $\langle 1\,1\,0 \rangle$ crystalline direction and with the racetracks in the $\langle 1\,0\,0 \rangle$ direction. The measurements were repeated several times. First, the chip was manually placed in the setup. Then resonators with different widths of the straight waveguide were automatically measured. The strain of the racetrack was increased and decreased from 0 to approximately 275 microstrain, with 6 steps in each direction [see Fig. 2(a)]. The transmittance spectrum was recorded for each applied strain, and the resonance position λ_m that started closest to λ_c was extracted. The effective group index $\langle n_g \rangle$ was also extracted from this spectrum. For each value of applied strain, the measured load L and the position of the linear stage Y were recorded. Per measurement set of increasing and decreasing strain, the resonance shift per displacement of the load cell, $\partial\lambda_m/\partial Y$, was obtained from a linear fit, and so was the relation between the displacement and the applied load, $\partial Y/\partial L$. We observed that both relations were indeed linear in this regime. The strain-induced resonance shift is then

$$\frac{\partial\lambda_m}{\partial S_z} = \frac{\partial\lambda_m}{\partial Y} \cdot \frac{\partial Y}{\partial L} \cdot \frac{\partial L}{\partial S_z} \tag{17}$$

in which the first two terms on the right-hand side are measured and the last term is calculated from (16).

The relation between the displacement of the load cell and the measured load can be interpreted as the resistance of the chip and setup to bending. The average value for the chip with the racetracks in the $\langle 1\,1\,0 \rangle$ direction is $\partial Y/\partial L = 0.128$ μm/mN and the average value for the chip with the racetracks in the $\langle 1\,0\,0 \rangle$ direction $\partial Y/\partial L = 0.135$ μm/mN.

[1] E_i is the Young's modulus along axis i.

[2] ν_{ij} is the Poisson's ratio that corresponds to a contraction in direction j when an extension is applied in direction i.

D. Numerical Mode Solver

For the analysis of the measurements, we calculated the effective index at zero strain, $n_e(\rho, \lambda_c, 0)$ using the film mode matching method in FimmWave [26]. Also the effective group index $n_g(\rho)$ at λ_c was calculated using this mode solver. The track-averaged effective index $\langle n_e \rangle$ and group index $\langle n_g \rangle$ are then straightforward to calculate.

E. Measurement Uncertainty Analysis

The uncertainty in the measurements was estimated following the guidelines of [29]. The relative errors of the three terms on the right-hand side of (17) are added quadratically, as they are independent. The chips with the racetrack resonators in the $\langle 1\,1\,0 \rangle$ and $\langle 1\,0\,0 \rangle$ directions were placed in the mechanical setup and measured 6 and 5 times, respectively.

1) $\partial\lambda_m/\partial Y$: The value for $\partial\lambda_m/\partial Y$ is averaged over the repetitive measurements, and the uncertainty is estimated as the standard deviation. The relative uncertainty did not significantly depend on the width of the waveguide, and the maximum relative uncertainty (of all widths) is used. The uncertainty for the chips with the waveguides in the $\langle 1\,1\,0 \rangle$ and $\langle 1\,0\,0 \rangle$ directions are 3.1% and 1.1%, respectively. The measurement-to-measurement difference mainly originated from repositioning the chip in the setup, which was done before each measurement. Repeating a measurement without repositioning the chip in the setup gives a measurement-to-measurement difference which is negligible. We could not attribute this difference to a slight tilt of the chip with respect to the setup (around the *y*-direction). We do not fully understand why the uncertainty in the $\langle 1\,1\,0 \rangle$ direction is higher, but the strong angle dependency of Poisson's ratio around the $\langle 1\,1\,0 \rangle$ direction may play a role. Also, we had to reassemble the setup between various $\langle 1\,1\,0 \rangle$ measurements, while the measurements of the $\langle 1\,0\,0 \rangle$ chip were performed consecutively in a mainly empty laboratory.

2) $\partial Y/\partial L$: The value of $\partial Y/\partial L$ did not significantly depend on the position of the chip in the setup. All measurements (for different widths of the waveguide, and repetitions of the measurements) are averaged to obtain $\partial Y/\partial L$. The statistical uncertainty (arising from random fluctuations) is estimated as the standard deviation, and the systematic uncertainty of the system (load cell, load cell voltage source, and A/D converter) is estimated as 3%. The standard deviation of the 30 measurements in the $\langle 1\,1\,0 \rangle$ direction is 2.8%, and the standard deviation of the 45 measurements in the $\langle 1\,0\,0 \rangle$ direction is 0.7%. This difference can be explained by the fact that we increased the integration time of the read-out of the load cell from 50 samples at 1 kHz for the $\langle 1\,0\,0 \rangle$ direction measurements to 1000 samples at 1 kHz for the $\langle 1\,1\,0 \rangle$ direction measurements. The output voltage of the load cell is a few mV, which required this longer integration time of our A/D converter (National Instruments USB-6251 DAQ). The uncertainties of $\partial Y/\partial L$ are thus 5.8% and 3.7% for the chips with the racetracks in the $\langle 1\,1\,0 \rangle$ and $\langle 1\,0\,0 \rangle$ directions, respectively.

3) $\partial L/\partial S_z$: The mechanics of the setup is described by (16). The material properties, dimensions, and uncertainties that are used in this equation are listed in Table I. The uncertainty σ of a quantity whose uncertainty is estimated as a maximum deviation u is given by $\sigma = u/\sqrt{3}$ [29]. In the computation of the uncertainty of $\partial L/\partial S_z$, we have treated all uncertainties as independent and approximated the influence of all the uncertainties as linear.

TABLE I
MATERIAL PROPERTIES, DIMENSIONS, AND ESTIMATED UNCERTAINTIES OF MECHANICAL SETUP

Quantity	Value	Uncertainty	
$E_z/(1-\nu_{xz}\nu_{zx})$, <110>	170 GPa[a]	4 GPa	2.5%[b]
$E_z/(1-\nu_{xz}\nu_{zx})$, <100>	141 GPa[a]	4 GPa	2.5%[b]
a_1	156 mm	0.3 mm	0.2%[c]
a_2	24 mm	0.03 mm	0.1%[d]
a_3	5 mm	0.03 mm	0.6%[d]
a_4	20 mm	0.03 mm	0.1%[d]
Chip W	24 mm	0.3 mm	1.2%[c]
Chip H	0.675 mm	0.01 mm	1.7%[e]
$\partial L/\partial S_z$, <110>	12.7 mN/μstrain	0.6 mN/μstrain	4.7%
$\partial L/\partial S_z$, <100>	10.5 mN/μstrain	0.5 mN/μstrain	4.7%

[a] From [21].
[b] Estimated.
[c] Measured with digital electronic calipers, maximum error 0.5 mm.
[d] Estimated fabrication uncertainty, maximum error 0.05 mm.
[e] Measured with digital electronic calipers, maximum error 0.02 mm.

4) Group Index $\langle n_g \rangle$: We found that the track-averaged effective group index does not depend on the applied strain. Therefore all measurements of a device are averaged, and the uncertainty is estimated as the standard deviation. These where 78 and 65 measurements for the racetracks in the $\langle 1\,1\,0 \rangle$ direction and $\langle 1\,0\,0 \rangle$ directions, respectively. The relative uncertainty did not depend much on the width of the straight waveguide in the racetrack nor on the crystalline orientation, so that we have used the maximum of 0.03%.

5) Effective Index $\langle n_e \rangle$: In the analysis of the measurements, we calculated the effective index with a numerical mode solver. We do not know the uncertainty, as it is mostly related to the difference between the simulated waveguide and the fabricated waveguide. Therefore, we estimated the uncertainty in the effective index as the difference between the measured effective group index $\langle n_g \rangle$ and the track-averaged group index as calculated with the same mode solver (see Fig. 5).

V. CHARACTERIZATION

We characterized two chips with long racetrack resonators; one chip with the resonators in the $\langle 1\,1\,0 \rangle$ silicon crystalline direction and one with the resonators in the $\langle 1\,0\,0 \rangle$ direction. A strain S_z was applied to the top surface of the chips, where the resonators are placed. The strain was increased to approximately 275 microstrain, and then decreased to zero strain in steps of approximately 45 microstrain. Per applied strain, the transmission spectrum of the resonator was recorded, as is shown in Fig. 2(a). The wavelength of the resonance dip which started closest to 1550 nm is extracted from each of the spectra, and plotted versus the applied strain in Fig. 2(b). The shift per applied strain $\partial\lambda_m/\partial S_z$ is obtained from a linear fit. This is done for racetracks with different widths, and the resonance shifts per strain are presented in Fig. 4. It can be seen that the racetracks

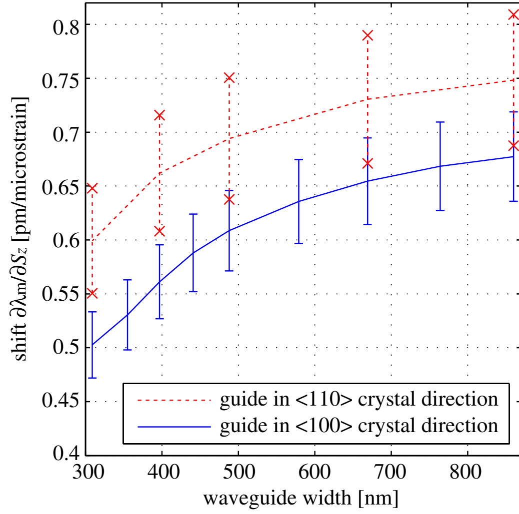

Fig. 4. Measured resonance shift per applied strain $\partial\lambda_m/\partial S_z$, with resonance wavelength λ_m and strain S_z.

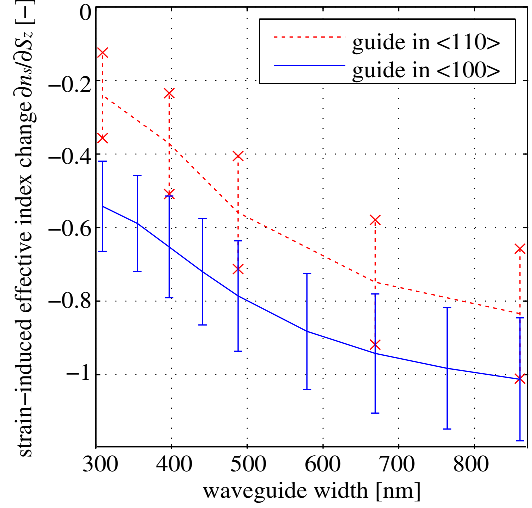

Fig. 6. Change in effective index of a straight waveguide, n_s, due to a strain, S_z, applied in the direction of the guide.

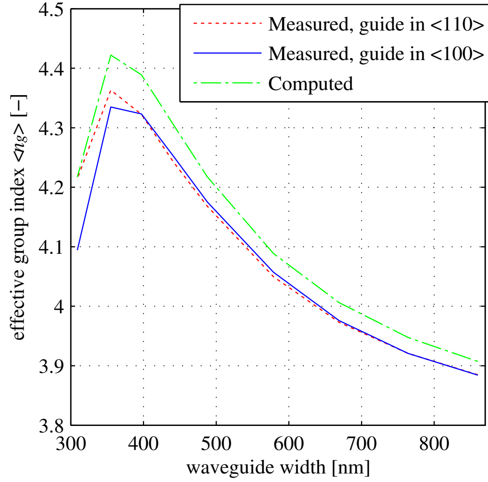

Fig. 5. Measured and calculated track-averaged effective group indices $\langle n_g \rangle$. Measured for racetracks in the $\langle 1\,0\,0 \rangle$ and in the $\langle 1\,0\,0 \rangle$ silicon crystalline directions.

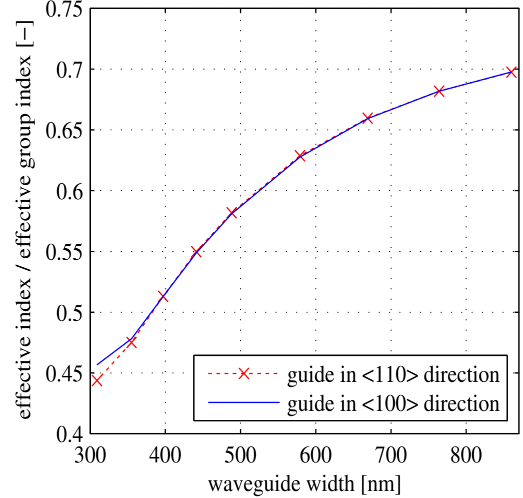

Fig. 7. Influence of dispersion on the strain-induced resonance shift, $n_s/\langle n_g \rangle$. Effective index n_s calculated with the mode solver. Track-averaged effective group index $\langle n_g \rangle$ is measured.

in the $\langle 1\,1\,0 \rangle$ direction are slightly more sensitive than the tracks in the $\langle 1\,0\,0 \rangle$ direction, and that the resonators with wider waveguides are more sensitive to strain than the ones with narrower waveguides widths. The latter can be attributed to the dispersion in the waveguide, as shown in Section VI. The estimated uncertainties are with respect to the absolute value of λ_m/S_z, and a large part of the uncertainty is a systematic bias and equal for all measurements. Considering only the statistical (or random) uncertainties, we found that the racetracks in the $\langle 1\,1\,0 \rangle$ and $\langle 1\,0\,0 \rangle$ directions have a significantly different shift in resonance.

The track-averaged effective group indices $\langle n_g \rangle$ were also extracted from the spectra and are presented in Fig. 5. We also calculated the effective group index with the numerical mode solver. The calculated and measured track-averaged effective group indices agree within 3%.

The change in effective index due to strain, $\partial n_e/\partial S_z$, is calculated using (10). We measured the resonance shift $\partial\lambda_m/\partial S_z$ and the effective group index $\langle n_g \rangle$, and we calculated the effective index n_s of the straight waveguide with the numerical mode solver. The resulting $\partial n_s/\partial S_z$ is shown in Fig. 6.

VI. Analysis

In this section, we interpret the measured shift and indicate the contributions of different physical effects: the elongation of the track, the change in effective index and the dispersion of the waveguide. Equation (13) shows how these effects shift the resonance wavelength. The effect of the elongation of the track (λ_c) and the effect of the change in effective index are added. The change in effective index $\partial n_s/\partial S_z$ is negative, so the two effects oppose each other. The dispersion of the waveguide, n_s/n_g, is smaller than unity, and thus damps the shift. Fig. 7 presents $n_s/\langle n_g \rangle$, in which it can be seen that this damping is stronger for small waveguides. Fig. 8 presents the resonance wavelength

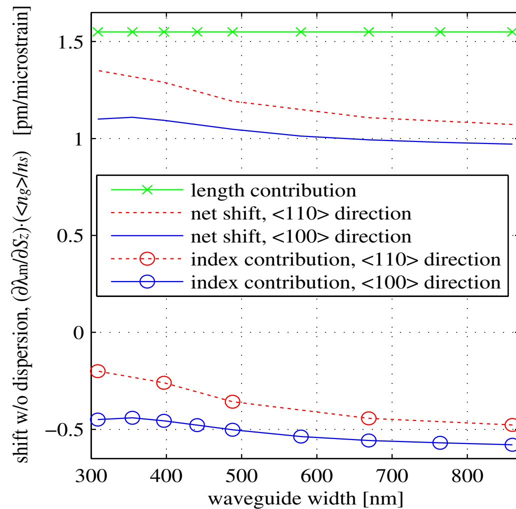

Fig. 8. The hypothetical strain-induced shift in resonance in which the dispersion is excluded. The two different contributions to this shift (track-length change and effective-index change) are shown. Results for the racetracks in the $\langle 1\,1\,0 \rangle$ and the $\langle 1\,0\,0 \rangle$ directions are shown.

shift with dispersion excluded. The shift due to the change in the effective index increases (in magnitude) with increasing width of the guide. The higher resonance shift for wider waveguides $\partial\lambda_m/\partial S_z$ is thus due to the dispersion, and not due to the change in effective index of the waveguide.

VII. Conclusion

We measured the strain-induced shift of the resonances of optical racetrack resonators in silicon-on-insulator technology. For waveguides with a width of 400 nm, the resonance wavelength shift per applied strain is 0.55 pm/microstrain when the racetrack is parallel to the $\langle 100 \rangle$-direction of the silicon crystal, and 0.66 pm/microstrain when the racetrack is parallel to the $\langle 110 \rangle$-direction. We observed largest sensitivity for wider waveguides; a racetrack with 860 nm wide waveguides oriented in the $\langle 110 \rangle$-direction has a resonance shift of 0.75 pm/microstrain. We have studied elongations up to 275 microstrain, and observed a linear relation between the resonance wavelength and the applied strain.

The effect of the strain-induced increase in track circumference and the effect of the strain-induced change in waveguide effective index oppose each other. The effect of the strain-induced increase in circumference is about three times larger than the effect of the change in effective index. The strong dispersion in the sub-wavelength silicon waveguides lowers the change in wavelength shift approximately by a factor two. In fact, the lower dispersion of the wider waveguides is the reason that these devices are more sensitive.

This paper addressed how micro-ring resonators transduce an applied strain into a shift of their optical resonance wavelengths. Sensor MEMS or MOEMS consist, next to the transducer, also of a mechanical structure that acts on the transducer and an interrogation system that reads the transducer. A variety of interrogation concepts exist for monitoring the shift in the resonances of optical resonators [30]–[36]. The detection limit of MOEMS sensors depends on the designs of the mechanical structure and the interrogation system. These designs are application specific as they depend, for example, on the bandwidth of the measured signal (e.g., [12] presents the design of an ultrasound sensor).

In this work, we have characterized a novel type of optical strain sensors which can be integrated in micro-electro-mechanical systems (MEMS). We believe these sensors open opportunities in different fields of applications such as in the medical, petrochemical, or oil&gas markets, by offering specific advantages such as high-speed readout over kilometer distances, integrated optical multiplexing, and small device size. Moreover, by removing the need for galvanic connections, susceptibility to electromagnetic disturbance is eliminated.

Acknowledgment

The authors would like to acknowledge the EU-funded ePIXfab consortium for the fabrication of the photonic devices, with special thanks to Dr. P. Dumon and Dr. A. Khanna of IMEC (Leuven, Belgium) for the technical support. At TNO (Delft, The Netherlands), we would like to thank J. H. van den Berg for post-processing the chips, Dr. E. van Veldhoven for the helium ion microscope (HIM) images, E. Tabak for the mechanical design and fabrication of the strain setup, and Dr. P. J. Harmsma, R. A. Nieuwland, and J. J. M. Groote Schaarsberg for the support in the photonics lab. We thank R. Pols, T. Zuidwijk, and R. C. Horsten of the Optics Research Group of Delft University of Technology for the support with the automation of the setup. We thank Dr. S. M. García Blanco of the University of Twente (The Netherlands) for the collaboration regarding the internship of P. M. Muilwijk.

References

[1] A. A. Barlian, W.-T. Park, J. Mallon, A. Rastegar, and B. Pruitt, "Review: Semiconductor piezoresistance for microsystems," *Proc. IEEE*, vol. 97, no. 3, pp. 513–552, Mar. 2009.

[2] P. Muralt and J. Baborowski, "Micromachined ultrasonic transducers and acoustic sensors based on piezoelectric thin films," *J. Electroceram.*, vol. 12, no. 1–2, pp. 101–108, 2004.

[3] P. Dumon, W. Bogaerts, A. Tchelnokov, J.-M. Fedeli, and R. Baets, "Silicon nanophotonics," *Future Fab Int.*, vol. 25, pp. 29–36, Apr. 2008.

[4] J. Pozo, P. Kumar, D. M. R. Lo Cascio, A. Khanna, P. Dumon, D. Delbeke, R. Baets, M. Fournier, J.-M. Fedeli, L. Fulbert, L. Zimmermann, B. Tillack, H. Tian, T. Aalto, P. O"Brien, D. Deptuck, J. Xu, X. Zhang, and D. Gale, "Essential: Epixfab services specifically targeting (sme) industrial takeup of advanced silicon photonics," in *Proc. 14th Int. Conf. Transp. Opt. Netw.*, 2012, pp. 1–3.

[5] D. Taillaert, W. Van Paepegem, J. Vlekken, and R. Baets, "A thin foil optical strain gage based on silicon-on-insulator microresonators," in *Proc. SPIE*, 2007, vol. 6619, p. 661914.

[6] W. J. Westerveld, J. Pozo, P. J. Harmsma, R. Schmits, E. Tabak, T. C. van den Dool, S. M. Leinders, K. W. van Dongen, H. P. Urbach, and M. Yousefi, "Characterization of a photonic strain sensor in silicon-on-insulator technology," *Opt. Lett.*, vol. 37, no. 4, pp. 479–481, Feb. 2012.

[7] X. Zhao, J. M. Tsai, H. Cai, X. M. Ji, J. Zhou, M. H. Bao, Y. P. Huang, D. L. Kwong, and A. Q. Liu, "A nano-opto-mechanical pressure sensor via ring resonator," *Opt. Express*, vol. 20, no. 8, pp. 8535–8542, Apr. 2012.

[8] E. Hallynck and P. Bienstman, "Integrated optical pressure sensors in silicon-on-insulator," *IEEE Photon. J.*, vol. 4, no. 2, pp. 443–450, Apr. 2012.

[9] S. M. C. Abdulla, P. J. Harmsma, R. A. Nieuwland, J. Pozo, M. Lemmen, H. Sadeghian, J. H. van den Berg, P. Bodis, and P. Buskens, "Soi based

mechano-optical pressure sensor using a folded microring resonator," in *Proc. 9th Nanomechan. Sensing Workshop,*, Mumbai, India, Jun. 2012, pp. 80–81.
[10] C. D. Liapis, K. Balzer, F. Benedetti-Valentini, and J. Fernandes e Fernandes, *Vascular Surgery*, (European Manual of Medicine). Berlin, Germany: Springer-Verlag, 2007.
[11] C. L. de Korte, H. H. G. Hansen, and A. F. W. van der Steen, "Vascular ultrasound for atherosclerosis imaging," *Interf. Focus*, vol. 1, no. 4, pp. 565–575, 2011.
[12] S. M. Leinders, W. J. Westerveld, J. Pozo, H. P. Urbach, N. de Jong, and M. D. Verweij, "Membrane design of an all-optical ultrasound receiver," in *Proc. IEEE Int. Ultrason. Symp.*, 2013.
[13] C. W. Wong, P. T. Rakich, S. G. Johnson, M. Qi, H. I. Smith, E. P. Ippen, L. C. Kimerling, Y. Jeon, G. Barbastathis, and S.-G. Kim, "Strain-tunable silicon photonic band gap microcavities in optical waveguides," *Appl. Phys. Lett.*, vol. 84, no. 8, pp. 1242–1244, 2004.
[14] B. T. Tung, H. M. Nguyen, D. V. Dao, S. Rogge, H. W. M. Salemink, and S. Sugiyama, "Strain sensitive effect in a triangular lattice photonic crystal hole-modified nanocavity," *IEEE Sens. J.*, vol. 11, no. 11, pp. 2657–2663, Nov. 2011.
[15] W. N. Ye, D.-X. Xu, S. Janz, P. Cheben, M.-J. Picard, B. Lamontagne, and N. G. Tarr, "Birefringence control using stress engineering in silicon-on-insulator (SOI) waveguides," *J. Lightwave Technol.*, vol. 23, no. 3, pp. 1308–1318, 2005.
[16] L. Fan, L. T. Varghese, Y. Xuan, J. Wang, B. Niu, and M. Qi, "Direct fabrication of silicon photonic devices on a flexible platform and its application for strain sensing," *Opt. Express*, vol. 20, no. 18, pp. 20 564–20 575, 2012.
[17] R. S. Jacobsen, K. N. Andersen, P. I. Borel, J. Fage-Pedersen, L. H. Frandsen, O. Hansen, M. Kristensen, A. V. Lavrinenko, G. Moulin, H. Ou, C. Peucheret, B. Zsigri, and A. Bjarklev, "Strained silicon as a new electro-optic material," *Nature*, vol. 441, pp. 199–202, 2006.
[18] M. Cazzanelli, F. Bianco, E. Borga, G. Pucker, M. Ghulinyan, E. Degoli, E. Luppi, V. Véniard, S. Ossicini, D. Modotto, S. Wabnitz, R. Pierobon, and L. Pavesi, "Second-harmonic generation in silicon waveguides strained by silicon nitride," *Nature Mater.*, vol. 84, pp. 148–154, 2012.
[19] J. Cai, Y. Ishikawa, and K. Wada, "Strain induced bandgap and refractive index variation of silicon," *Opt. Express*, vol. 21, no. 6, pp. 7162–7170, Mar. 2013.
[20] A. Yariv, "Universal relations for coupling of optical power between microresonators and dielectric waveguides," *Electron. Lett.*, vol. 36, no. 4, pp. 321–322, 2000.
[21] M. A. Hopcroft, W. D. Nix, and T. W. Kenny, "What is the Young's modulus of silicon?" *J. Microelectromech. Syst.*, vol. 19, no. 2, pp. 229–238, 2010.
[22] J. M. Gere and S. P. Timoshenko, *Mechanics of Materials*, 4th ed. London, U.K.: Stanley Thornes, 1999.
[23] S. P. Timoshenko and S. Woinowsky-Krieger, *Theory of Plates and Shells*, 2nd Reissue ed. New York, NY, USA: McGraw-Hill, 1987.
[24] D. Taillaert, W. Bogaerts, P. Bienstman, T. Krauss, P. van Daele, I. Moerman, S. Verstuyft, K. de Mesel, and R. Baets, "An out-of-plane grating coupler for efficient butt-coupling between compact planar waveguides and single-mode fibers," *IEEE J. Quantum Electron.*, vol. 38, no. 7, pp. 949–955, Jul. 2002.
[25] W. J. Westerveld, H. P. Urbach, and M. Yousefi, "Optimized 3-D simulation method for modeling out-of-plane radiation in silicon photonic integrated circuits," *IEEE J. Quantum Electron.*, vol. 47, no. 5, pp. 561–568, May 2011.
[26] Photon Design (Oxford, U.K.). (2012, Sep.). *Fimmwave, a powerful waveguide mode solver*. [Online]. Available: http://www.photond.com/products/fimmwave.htm
[27] J. J. Moré, "The levenberg-marquardt algorithm: Implementation and theory," in *Numerical Analysis*, vol. 630, (Lecture Notes in Mathematics), G. Watson, Ed. Berlin/Heidelberg, Germany: Springer-Verlag, 1978, pp. 105–116.
[28] T. O'Haver. (2012, Sep.). Findpeaks matlab function by Tom O'Haver. [Online]. Available: http://terpconnect.umd.edu/~toh/
[29] S. E. Angad Gaur and E. Lagendijk, "Inleiding practicum technische natuurwetenschappen," Reader, Delft University of Technology, Faculty of Applied Sciences, Delft, The Netherlands, 2002 (follows the Guide to the Expression of Uncertainty in Measurement (ISO/IEC Guide 98:1993)).
[30] P. J. Harmsma, H. Sadeghian, S. M. C. Abdulla, and R. A. Nieuwland, "Wavelength noise in ring resonator sensors," presented at IEEE Symp. Photon. Soc. Benelux Chapter, Mons, Belgium, 2012.
[31] P. J. Harmsma, J.-P. Staats, D. M. R. Lo Cascio, and L. K. Cheng, "Three-port interferometer in silicon-on-insulator for wavelength monitoring and displacement measurement," presented at the Lasers Electro-Opt. Eur. (CLEO EUROPE/EQEC) Conf. 12th Eur. Quantum Electron. Conf., Munich, Germany, 2011.
[32] C. Mesaritakis, A. Argyris, E. Grivas, A. Kapsalis, and D. Syvridis, "Adaptive interrogation for fast optical sensing based on cascaded micro-ring resonators," *IEEE Sens. J.*, vol. 11, no. 7, pp. 1595–1601, Jul. 2011.
[33] N. Yebo, W. Bogaerts, Z. Hens, and R. Baets, "On-chip arrayed waveguide grating interrogated silicon-on-insulator microring resonator-based gas sensor," *IEEE Photon. Technol. Lett.*, vol. 23, no. 20, pp. 1505–1507, Oct. 2011.
[34] J. Song, L. Wang, L. Jin, X. Xia, Q. Kou, S. Bouchoule, and J.-J. He, "Intensity-interrogated sensor based on cascaded Fabry-Perot laser and microring resonator," *J. Lightwave Technol.*, vol. 30, no. 17, pp. 2901–2906, 2012.
[35] T. Claes, W. Bogaerts, and P. Bienstman, "Vernier-cascade label-free biosensor with integrated arrayed waveguide grating for wavelength interrogation with low-cost broadband source," *Opt. Lett.*, vol. 36, no. 17, pp. 3320–3322, Sep. 2011.
[36] L. Jin, M. Li, and J.-J. He, "Optical waveguide double-ring sensor using intensity interrogation with a low-cost broadband source," *Opt. Lett.*, vol. 36, no. 7, pp. 1128–1130, Apr. 2011.

Wouter J. Westerveld (M'10) received the M.Sc. degree in applied physics (*cum laude*) in 2009 from the Delft University of Technology, Delft, The Netherlands, where he is currently working toward the Ph.D. degree in collaboration with TNO. His research interests include applied physics in general and in silicon integrated micro opto-mechanical systems in particular. Mr. Westerveld was a board member of the Student Association for Applied Physics (VvTP) at Delft University in 2004–2005. He was the Secretary (2011) and the Chairman (2012) of the Student Board of the IEEE Photonics Society Benelux Chapter. He is certified Project Management Associate (IPMA Level D).

Suzanne M. Leinders received the M.Sc. degree in applied physics from the Delft University of Technology, Delft, The Netherlands, in 2010, where she is currently working toward the Ph.D. degree. Her research interest includes medical acoustical imaging.

Pim M. Muilwijk is working toward the M.Sc. degree in nanotechnology at the University of Twente, Enschede, The Netherlands. He is currently holding a position as a Research Scientist in the nanoinstrumentation group of the Dutch Organization for Applied Scientific Research (TNO), Delft, The Netherlands. His research at the University of Twente involves developing fabrication technologies for double tungstate gain materials while at TNO he works on contamination control of vacuum systems. Mr. Muilwijk was a member of the accreditation committee of the nanoscience curriculum at the University of Groningen in 2012.

Jose Pozo received the Graduate degree from the Universidad Publica de Navarra, Madrid, Spain, and Vrije Universiteit Brussel, Belgium, in electrical engineering with M.Sc. degree in telecommunications in 2002, and received the Ph.D. degree from the University of Bristol, U.K., in 2006 on dilute nitride lasers for broadband communications. In 2007, he joined the COBRA Research Institute (Eindhoven, The Netherlands) where he worked as a Postdoctoral Researcher on the study of chaotic semiconductor lasers as emitter and receivers of a chaos-encrypted communication link; and on the development of a novel concept for an integrated tunable laser based on filtered feedback. In 2010, he joined TNO as EU Proposal Coordinator and Scientist Specialist in integrated optics. Dr. Pozo is member of the board of IEEE Benelux Photonics Society since 2012.

Teun C. van den Dool received the Master's degree in applied physics (*cum laude*) from the University of Groningen, Groningen, The Netherlands, in 1989. He joined the TNO Institute of Applied Physics, Delft, The Netherlands, where he has been working as a Systems Architect and an Engineer on a multitude of subjects ranging from active noise and vibration control to development of instruments for semicon, astronomy, and earth observation space instruments. He currently holds the position of Principal Scientist at TNO, as such contributing to the definition of future developments at TNO. His research interests include opto-mechatronic system design and realization.

Martin D. Verweij (M'10) received the M.Sc. degree (*cum laude*) in 1988 and the Ph.D. degree in 1992, both from the Delft University of Technology, Delft, The Netherlands. From 1993 to 1997, he was a Research Fellow of the Royal Netherlands Academy of Arts and Sciences. In 1998, he became an Associate Professor in the Laboratory of Electromagnetic Research, Delft, Delft University of Technology, where he joined the Laboratory of Acoustical Wavefield Imaging in 2011. His research interests include the theoretical modeling and numerical simulation of medical ultrasound. Dr. Verweij is an Associate Editor of the *Journal of the Acoustical Society of America*.

Mirvais Yousefi (M'99) was born in Kabul, Afghanistan, and received the M.Sc. degree in physics from the University of Lund, Lund, Sweden, in 1998. He continued toward the Ph.D. degree at the Vrije Universiteit Amsterdam in 2003. Since then he has worked as Postdoctoral Researcher at the Vrije Universiteit Amsterdam, the Vrije Universiteit Brussel, and the COBRA Institute in Eindhoven, and as Top Technologist at TNO in Delft. He owns currently Photonic Sensing Solutions in Amsterdam. His major research interests include laser dynamics and commercial photonic sensing technology. Dr. Yousefi is the Chairman of the IEEE Benelux Photonics Society.

H. Paul Urbach received the Graduate degree in 1981 from the University of Groningen, The Netherlands, and completed in 1986 a Ph.D. thesis at the same university on the optimization of hydrodynamic propulsion. He joined the Philips Research Laboratory in Eindhoven, The Netherlands, in 1986. In 1994, he became Principal Scientist at Philips Research Laboratory. In 2000, he became Part-Time Professor in diffraction optics at the Delft University of Technology. Since January 2008, he has been a Full Professor and the Head of the Optics Research Group of the same university. Dr. Urbach is President-Elect of the European Optical Society.